Journal of Materials Chemistry C

PAPER

View Article Online
View Journal | View Issue

Cite this: J. Mater. Chem. C, 2017, 5, 902

Understanding surface chemistry during $MAPbI_3$ spray deposition and its effect on photovoltaic performance†

Conor Rocks,*[a] Vladimir Svrcek,[b] Paul Maguire[a] and Davide Mariotti*[a]

Received 8th November 2016,
Accepted 3rd January 2017

DOI: 10.1039/c6tc04864a

www.rsc.org/MaterialsC

In recent years there has been significant research into organic–inorganic halide perovskites for photovoltaic applications and has resulted in power conversion efficiencies greater than 20%. A number of deposition techniques have been utilized to produce high quality perovskite films including thermal evaporation, single and two-step spin coating and vapor assisted processes. However, these laboratory based fabrication methods are not well matched with low costing, roll to roll processing that is associated with large scale manufacture. In this work we use a low costing and rapid spray coating technique to fabricate solution processed $MAPbI_3$ films with controlled film thickness achieved through modifying concentration/spray volume. Investigation into the chemical composition and film morphology showed differing surface chemistries for the different film thicknesses, altering the surface morphology from large micro grained structures to small distorted grain arrangements. We have then implemented spray deposited films into solar devices (ITO/TiO_2/$MAPbI_3$/Au) and have studied the current density–voltage (*JV*) characteristics including light soaking effects. Through optimizing the absorber thickness the short-circuit current density is increased from 4.9 mA cm^{-2} to 22.3 mA cm^{-2}, increasing overall power conversion efficiency by a factor >5. Investigation into the performance of devices under continued illumination showed an inverse relationship existed between low efficiency (thick) $MAPbI_3$ films and high efficiency (thin) $MAPbI_3$ films, where the former displayed large increases in overall performance compared to the rapid degradation in the latter. We attribute device instabilities to the increase in defect density as a consequence of the spray-induced surface chemistry, leading to trap assisted recombination at the back electrode.

Introduction

Over recent years, organic–inorganic halide perovskites have received considerable attention due to their intense light absorption, greater charge diffusion lengths and low exciton binding energies.[1] Rapid developments in device engineering along with material processing have led to power conversion efficiencies greater than 20%.[2,3] The perovskite structure is typically represented by the general formula ABX_3, where in the case of organic–inorganic halide perovskites A is a small organic cation ($CH_3NH_3^+$), B is a metal cation (Pb^{2+}) and X is a monovalent halide anion (I^-). Variations in the metal and halide components have been demonstrated to impact the perovskites electronic structure, enabling bandgap tunability between 1.5 eV and 3.1 eV.[4] Despite the perovskites many enhanced opto-electronic properties, successful implementation into applications, mainly photovoltaic, has been hindered by a number of key operational issues. These issues arise from the complex nature of the perovskites intrinsic properties which are not yet fully understood. Under normal operating conditions, light soaking effects and hysteresis phenomena have been observed for perovskite solar cells.[5–9] Experimental studies have shown that both light soaking effect and hysteresis phenomena are related to the electrode interfaces in heterojunction perovskite devices. There is a general consensus that a number of mechanisms may be responsible and act simultaneously, such as reorientation of ferroelectric organic cations,[10] trapping/de-trapping of charge carriers,[11] lattice distortion-induced polarization and ion migration.[12,13] In order for perovskites enhanced properties to be successfully implemented into a range of applications, high quality thin films must be produced. Several deposition techniques including thermal evaporation,[14] single and two step spin coating[15,16] and vapor assisted processes[17] have been optimized to achieve high quality

[a] Nanotechnology & Integrated Bio-Engineering Centre (NIBEC), Ulster University, UK. E-mail: rocks-c2@email.ulster.ac.uk
[b] Research Center for Photovoltaics, National Institute of Advanced Industrial Science and Technology (AIST), Central 2, Umezono 1-1-1, Tsukuba, 305-8568, Japan

† Electronic supplementary information (ESI) available: XPS survey and N 1s core level scans of sprayed $MAPbI_3$ films, FTIR and Raman spectroscopy for atmospheric aging of pristine $MAPbI_3$. *JV* curves 0–6 minutes under illumination with plotted J_{SC} and V_{OC}. See DOI: 10.1039/c6tc04864a

perovskite films for use in high performing PV devices. However, these laboratory based fabrication methods for perovskite films are not well-matched with a low costing, roll to roll process that is typical for large scale manufacture.[18] A solution would be to develop a one-step spray coating approach, which has already been successfully exploited for a range of electronic devices such as light emitting diodes,[19] photo-detectors,[20] field effect transistors[21] and also photovoltaics.[22,23] However, challenges still exist to deploy spray coating for perovskite photovoltaics as for instance thin layers as required for optimal device performance are still difficult to achieve by spray. Nonetheless, a one-step spray coating method still presents technological relevance and advantages that are highly beneficial to industrial manufacture, such as the ability to simultaneously provide high throughput, efficient use of material and uniform film coverage. Additionally, control over directional deposition means that grains grow in a vertically aligned manner, resulting in low number of grain boundaries that could benefit overall charge transport properties. A main issue concerning the implementation of methylammonium lead iodide ($MAPbI_3$) as a feasible and efficient absorber for solar devices is its stability. Exposure to even ambient atmospheric conditions causes severe degradation of the $MAPbI_3$ film and their unique opto-electronic properties diminish as a consequence. Numerous works have established the effects of moisture and oxygen ingress into $MAPbI_3$ films and it is well understood that as MAI is evaporated solid PbI_2 remains on the film, which turns into a yellowish shade from the original dark colour. MAI can be further broken down to CH_3NH_2 (liquid) and HI (liquid) with the latter easily reacting with O_2 to form I_2 (solid) and H_2O (liquid) or decompose into I_2 (solid) and H_2 (gas).[24] In this work we use a low costing and scalable one-step spray technique to fabricate solution processed $MAPbI_3$ films. By changing the concentration of $MAPbI_3$ in DMF solution (0.25 M and 0.125 M) along with the spray volume (400 μL, 300 μL and 200 μL) we were able to control the film thickness. The surface chemistry of $MAPbI_3$ films induced during spraying are studied in detail using X-ray photoelectron spectroscopy (XPS) and indicates increased surface reactivity for reduced film thicknesses. A direct consequence is the accelerated decomposition from $MAPbI_3$ to $MAPbI_{2+x}/PbI_2$ where we highlight in detail the intermediate chemical phases that are formed during this transition together with surface morphology changes. The spray deposited films are used in solar devices with TiO_2 as an electron transfer/hole blocking layer and their current density–voltage (*JV*) characteristics are studied to include light soaking effects over a period of 0–6 min. This work provides in-depth details of changing surface chemistry as a result of the spray method, which highlights a more rapid degradation process at the surface of thinner films. The subsequent effect on the electronic band structure for spray produced $MAPbI_3$ films is also analysed in details.

Experimental section

Materials

Precursor materials triethanolamine, titanium(IV) isoperoxide and titanium(IV) oxide anatase nanopowder <25 nm diameter were purchased from Sigma-Aldrich and used as received. Methylammonium lead iodide ($CH_3NH_3PbI_3$) perovskite powder with 99% purity was purchased from Xi'an p-OLED.

Film deposition and device fabrication

Fabrication of compact TiO_2. Solution of TiO_2 was produced using a mixture of triethanolamine (0.39 g) and Titanium(IV) isoperoxide (1.56 mL) with ethanol (18 mL) before mixing at 40 °C for 2 hours then left overnight. The solution was then spin coated at 5000 rpm for 30 s on top of the indium-tin oxide (ITO) coated glass substrate followed by annealing the film at 300 °C (Fig. 1a.1 and 2).

TiO_2 mesoporous and $CH_3NH_3PbI_3$ thin film fabrication using one-step spray technique. A solution of 40 mg Titanium(IV) oxide anatase nanopowder <25 nm diameter and 20 mL of ethanol/DI-water (1 : 1) is mixed and sonicated for 30 minutes followed by an additional settling period of 30 minutes. 400 μL is then sprayed in air using an airbrush (pro series BD-132) *via* nitrogen gas flow at 1 bar pressure positioned 15 cm above a hot plate at 0° angle incident to substrate surface and annealed for 1 h at 150 °C to form a mesoporous TiO_2 layer (Fig. 1a.3). Methylammonium lead iodide ($CH_3NH_3PbI_3$) perovskite powder is mixed in dimethylformamide (DMF) at 60 °C at 0.25 M and 0.125 M (1 M = 0.619.9 g mL^{-1}) and using the same spray deposition technique with nitrogen gas flow and at 1 bar pressure the solution is sprayed in air on to mesoporous TiO_2 layer and annealed for 40 min at 100 °C (Fig. 1a.4). All samples were transferred directly to XPS vacuum chamber within minutes following the annealing procedure.

Deposition of metal contacts. Finally for use in photovoltaic device gold (Au) contacts are deposited using a Moorfield minilab DC/RF magnetron box sputter system using argon plasma at constant current of 0.15 A for 60 min with a working pressure of 1.5×10^{-2} mbar (Fig. 1a.5). Energy band diagrams show that TiO_2 film acts as an electron transport/hole blocking material with Au contact creating a Schottky barrier at the back electrode (Fig. 1b).

Characterization of sprayed $MAPbI_3$ films

Cross sectional scanning electron microscopy (SEM) was performed using a JEOL JSM-6010PLUS at 20 kV acceleration voltages. X-ray photoelectron spectroscopy (XPS) to determine surface chemical composition was performed using an X-ray source (Al = 1486 eV) and the Kratos AxisUltra DLD spectrometer with peak fitting performed using Kratos software. Current and voltage were 10 mA and 15 kV respectively with an operating pressure of 10^{-9} bar. Specific region scans were performed at a resolution of 0.05 eV and pass energy of 20 eV. X-ray spot size and hence capture area is equal to 400 μm^2 with a penetration depth of 10 nm. Calibration of obtained spectra was performed using the C 1s peak located at 284.8 eV. Attenuated total reflectance Fourier transform infra-red spectroscopy (FTIR) was performed and measured using a Thermo-scientific spectrometer. Spectra were obtained over a range of 600–3500 cm^{-1} at a 2 cm^{-1} resolution. Raman spectroscopy was carried out using an ISA Lab-ram 300 confocal spectroscope with a 632.8 nm

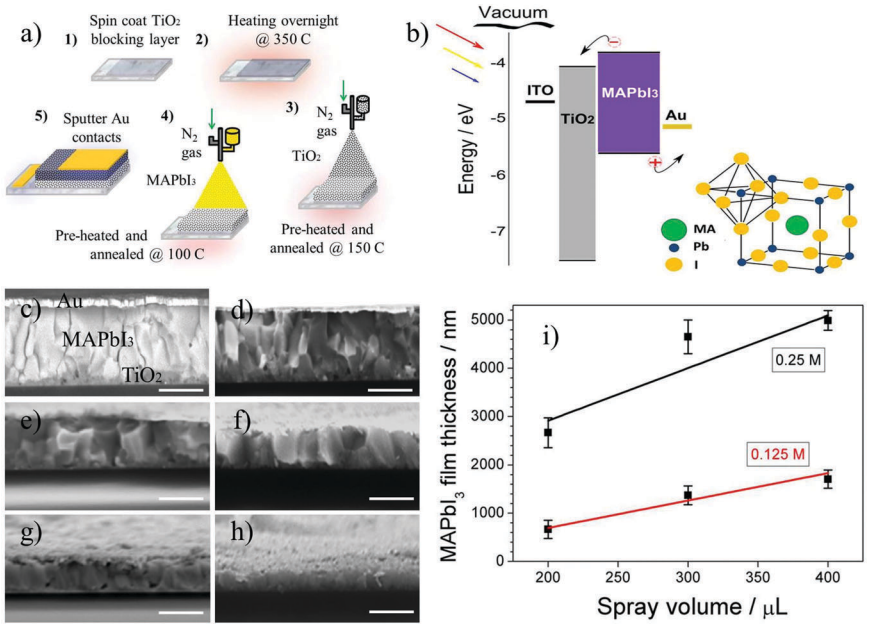

Fig. 1 (a) Fabrication steps for the synthesis of $MAPbI_3$ solar devices and (b) non-equilibrated band diagram for our cell architecture and (inset bottom right) unit cell for $MAPbI_3$ perovskite. (c–h) Cross sectional scanning electron microscopy (SEM) images of deposited $MAPbI_3$ on a mesoporous TiO_2 layer by a one-step spray method using the following $MAPbI_3$ in DMF concentration/spray volume: (c) 0.25 M/400 μL (d) 0.25 M/300 μL (e) 0.25 M/200 μL (f) 0.125 M/400 μL (g) 0.125 M/300 μL and (h) 0.125 M/200 μL. Scale bars 2.5 μm. (i) Measured $MAPbI_3$ film thickness using following deposition implementing set concentrations and spray volumes.

helium-neon laser to obtain spectra from 0 cm^{-1} to 500 cm^{-1} with 20 s exposure time and laser power of 10 mW. The Fermi level measurements are characterized using a scanning Kelvin probe system (KPTechnology) with a total of 20 measurements are taken across the sample surface and presented as a mean value with error bars representing standard deviation. Ultraviolet-visible (UV-Vis) absorption measurements are measured using a deuterium-halogen light source and an integrating sphere. Current density–voltage (*JV*) curves of devices incorporating sprayed $MAPbI_3$ films were recorded by a Keithley 6430 sub-FA sourcemeter unit under illumination 1.5 AM in air at ambient temperature. The applied bias varied from −1 V to 1 V in steps of 0.01 V at a scan rate 700 mV s^{-1} consistently for all devices.

Results

Varying $MAPbI_3$ film thickness

$MAPbI_3$ films of varying thickness were produced by changing concentration (0.25 M and 0.125 M) and spray volume (200 μL, 300 μL and 400 μL). To track the changes in film thickness the cross sectional scanning electron microscopy (SEM) images were taken (Fig. 1c–h). Fig. 1c image was captured using back scattered electrons and presented to differentiate between meso-TiO_2/$MAPbI_3$/Au layers. A number of measurements using a profilometer for compact TiO_2 and mesoporous TiO_2 show thicknesses of 32.76 nm ± 12.16 and 569.25 nm ± 145.02 nm respectively. A plot of film thickness *versus* spray volume for 0.25 M and 0.125 M concentrations of $MAPbI_3$ in DMF show that film thickness decreases in a linear fashion with decreasing spray volume (Fig. 1i). Error bars represent 8 measurements taking

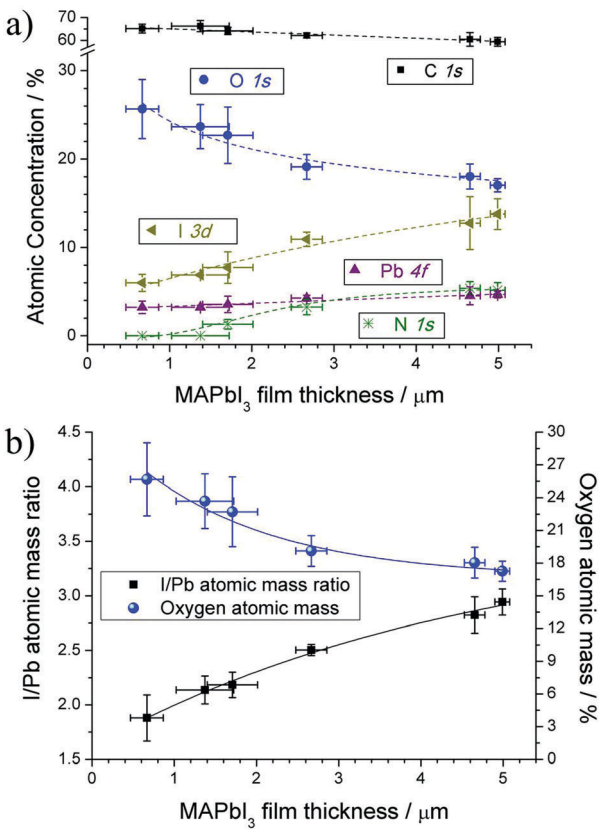

Fig. 2 (a) Atomic concentration of C 1s, O 1s, N 1s, Pb 4f and I 3d components in $MAPbI_3$ films as a function of film thickness, determined from XPS measurements with (b) quantified XPS results highlighting atomic mass ratio for I/Pb and oxygen atomic mass percentage for decreasing $MAPbI_3$ film thickness.

across full width of film in order to highlight the homogeneousness nature of deposition process.

Chemical analysis of $MAPbI_3$ films

The XPS spectra were recorded to investigate the elemental composition and understand the impact that decreasing film thickness may factor into the surface stability and durability of our sprayed $MAPbI_3$ films. The XPS survey spectrum (ESI†) for a typical $MAPbI_3$ perovskite shows peaks at binding energies of 532 eV, 401 eV and 284.8 eV corresponding to the photoelectron peaks of O 1s, N 1s and C 1s respectively. The doublet peaks of I and Pb are located around 618 eV and 137 eV, respectively, with their associated spin orbit splitting. To assess the chemical changes of our $MAPbI_3$ films produced at decreasing thicknesses, we recorded the high resolution photoelectron spectra of each sample. XPS spectra were calibrated to 284.8 eV according to the C 1s binding energy for adventitious (aliphatic) carbon.[25] The core level spectra obtained were fitted using Gaussian line shapes after linear background subtraction. The atomic concentrations for each specific region were determined from the integrated area under their peaks accounting for photoionization cross section and plotted as a function of $MAPbI_3$ film thickness (Fig. 2a); error bars in the *y*-axis represent average and standard deviation (SD) for 3 different spots across sample surface. There is a comparable reduction in the elemental composition for I 3d and N 1s components as the thickness of the $MAPbI_3$ film reduces. The elemental composition for C 1s increases slightly whereas the Pb 4f component decreases by a similar amount, also with decreasing thickness. Most noticeably is the increase in O 1s concentration for decreasing $MAPbI_3$ film thicknesses.

The atomic mass ratio of I/Pb and the total atomic mass percentage of O 1s *vs.* $MAPbI_3$ film thickness, calculated from the integrated areas under Pb 4f, I 3d and O 1s peaks, show a mirrored symmetry (Fig. 2b). As highlighted previously, for decreasing $MAPbI_3$ film thickness, the total atomic concentration of the I 3d peak decreased gradually relative to the total concentration of the Pb 4f peak. This reduction (we expect a 3 : 1 I/Pb ratio in the stoichiometric crystal) implies that the amount of surface oxygen species correlates directly with the decrease in iodide concentration for $MAPbI_3$ films.

C 1s core level spectra for our $MAPbI_3$ with I/Pb ratio closer to the stoichiometric 3 : 1 (*i.e.* thickness >2 μm, Fig. 2b) included three peaks located at 284.8 eV, 285.9 eV and 287 eV (Fig. 3a–c). The peak found at 284.8 eV is commonly used for calibration and is known as adventitious carbon or adsorbed surface hydrocarbon species from the atmosphere.[25] The peak located at 285.9 eV can be attributed to methyl carbons in the $MAPbI_3$ film or additionally adsorbed surface carbon singly bonded to a hydroxyl group.[26] An additional peak that corresponds to carbon doubly bonded to oxygen can be found at 287 eV, which is also attributed to surface contamination. As $MAPbI_3$ film thickness reduces (Fig. 3d–f, corresponding to <2 μm thickness), reducing the I/Pb surface ratio, a carbon peak located at 289 eV appears and can be assigned to $PbCO_3$ which confirms the formation of a carbonate as an additional by-product during the decomposition of $MAPbI_3$ to form solid PbI_2.[27]

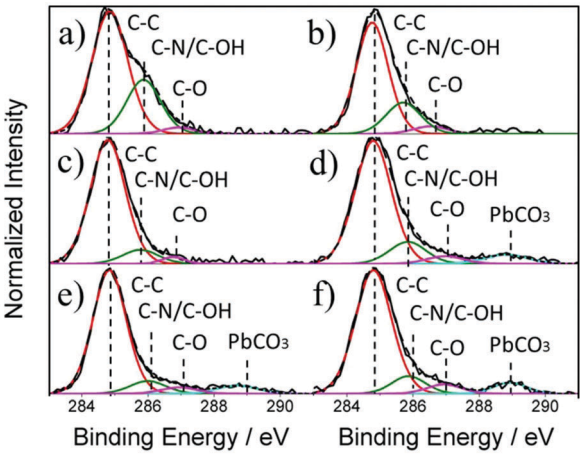

Fig. 3 XPS core level spectra for C 1s where (a–f) represents decreasing $MAPbI_3$ film thickness: (a) 4.99 μm, (b) 4.65 μm, (c) 2.67 μm, (d) 1.71 μm, (e) 1.37 μm and (f) 0.67 μm.

Fig. 4a–f shows the XPS analysis of the O 1s region for $MAPbI_3$ films of varying thickness. The O 1s spectra for our samples can be initially de-convoluted into two peaks found at 531.8 eV and 533.5 eV corresponding to O═C and O═C–O respectively.[28] These peaks are typical for most air exposed samples and are known as adventitious carbon, comprising of a variety of hydrocarbon species with both singly and doubly bound oxygen functionality. The appearance of a peak found at 530.4 eV (O′) is attributed mainly to weakly adsorbed OH^- and O^{2-} ions but has also been referenced as intercalated lattice O or $PbO/Pb(OH)_2$ like states.[27,28] $MAPbI_3$ films are known to be significantly affected by surface oxidation where chemisorbed or dissociated oxygen species can diffuse and distort the $MAPbI_3$ framework causing degradation. As the concentration of iodide ions reduces at the surface of our $MAPbI_3$ films, the intercalated oxygen (O^{2-}) can readily terminate Pb dangling bonds resulting in the formation

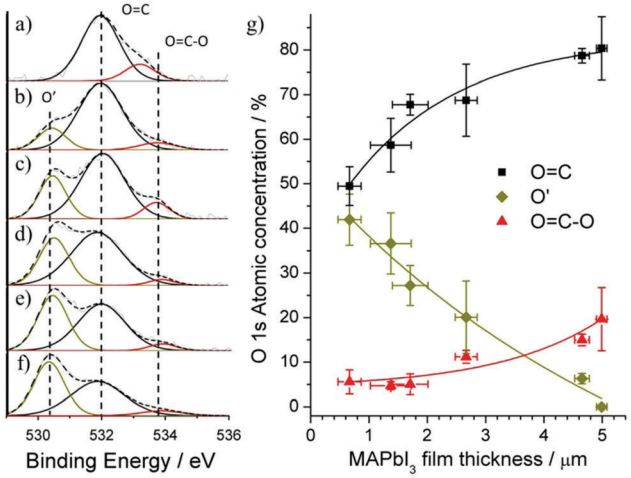

Fig. 4 (a) X-ray photoelectron spectroscopy analysis of the O 1s region for decreasing $MAPbI_3$ film thickness: (a) 4.99 μm, (b) 4.65 μm, (c) 2.67 μm, (d) 1.71 μm, (e) 1.37 μm and (f) 0.67 μm. (g) Summarized atomic mass concentration for each fitted component in the O 1s spectra.

of $PbO/Pb(OH)_2$ like states. However, through XRD measurements it has been highlighted that Pb–O bonds in $MAPbI_{2+x}$ do not lead to the formation of secondary phases of PbO.[29] The atomic mass percentages for our de-convoluted O 1s peaks was calculated from their integrated areas and plotted against $MAPbI_3$ film thickness (Fig. 4g). The decrease in the O′ component coupled with the Increase in O═C and O═C–O components, highlight the ability for adsorbed oxygen species to more easily diffuse into thin $MAPbI_3$ films.

Binding energy of metallic Pb is typically found at lower energies in the region 136.3–136.9 eV,[30] however during the perovskite formation there is a substantial alteration in Pb 4f core level due to the re-structuring of surface states to form Pb ions. The non-appearance of a metallic Pb state signifies strong charge transfer between Pb and I species to form donor–acceptor complexes. The Pb 6p valence state donates its excess unpaired electrons to the more electronegative iodide atoms where oxidation state Pb^{2+} is formed with iodide reducing to anion I_2^-.[28,31] An additional iodide ion bonded with organic MA^+ cation form weak van der Waals interaction with Pb–I framework to make up the PbI_6 octahedral within the perovskite lattice. It follows that the Pb 4f spectra of the $MAPbI_3$ films generally exhibit symmetrical peaks at 137.6 eV and 142.6 eV, corresponding to the spin orbit splitting of the Pb $4f_{7/2}$ and $4f_{5/2}$ components respectively that represent the Pb^{2+} cation in the $MAPbI_3$ structure.[32] The Pb $4f_{7/2}$ component of our $MAPbI_3$ films with decreasing thickness is presented in Fig. 5a–f; the peak at 142.6 eV is not shown here but remains constant throughout the samples. For thicker film (Fig. 5a and b), the Pb $4f_{7/2}$ component is present with no other peak. As the film thickness is reduced, there is significant broadening in the accompanying Pb 4f spectra (Fig. 5c and d) that allows for the fitting of an additional peak around 138.4 eV attributed to the PbI_2 component.[33] The intensity of this PbI_2 peak increases with decreasing $MAPbI_3$ film thickness while the peak corresponding to Pb^{2+} state (137.6 eV) decreases (Fig. 5c–f). It is worth mentioning that a peak corresponding to $PbO/Pb(OH)_2$ in the Pb 4f spectra has shown to also have a binding energy of around 138.4 eV[34] and therefore may overlap with the PbI_2 component. Reviewed literature highlights that $PbO/Pb(OH)_2$ and PbI_2 components can be found within binding energy ranges of 137.7–138.5 eV and 138.3–138.9 eV, respectively.[35–37] However, weakly adsorbed oxygen species (O^{2-}, OH^-) highlighted previously in O 1s spectra (BE = 530.4 eV, Fig. 4a–f) indicate that only constrained/amorphous $PbO/Pb(OH)_2$ like states may be formed due to the termination of Pb dangling bonds (iodide vacancies). Formation of crystalline PbO in the O 1s region is typically found at lower binding energies around 529 eV[38] and therefore the loss of iodine ions resulting in PbI_2 bonding arrangement is mainly responsible for the broadening observed in the Pb 4f spectra. Furthermore, the appearance of a third peak located at 139.1 eV is attributed to $PbC_2O_4/PbCO_3$ bonds, consistent with Fig. 3, and has recently been shown to be an additional oxidation by-product of $MAPbI_3$.[27] The overall carbon concentration was observed to increase while the overall Pb concentration decreased by a comparable amount for thin $MAPbI_3$ films (Fig. 2a): the C 1s/Pb 4f atomic ratio increased around 1.3 times with decreasing thickness. Since Pb cannot leave the film it can be concluded that surface polymerization produces a surface hydrocarbon layer, which may also limit the escape depth of Pb 4f photoelectrons. The fact that the carbonate ($PbC_2O_4/PbCO_3$) component is more pronounced in the C 1s core level spectra compared with the Pb 4f core level is due to the photo ionization cross section of C 1s electrons being around 100 times lower than the Pb 4f electrons. Fig. 5g summarizes the concentrations derived from Pb 4f spectra, which highlights drastic changes taking place at the surface of the sprayed film. Thick films (>2 μm) resembling a typical $MAPbI_3$ composition and thin films (<2 μm) exhibiting surface changes.

XPS for core level I 3d exhibits two intense peaks for thicker films, corresponding to doublets $3d_{5/2}$ and $3d_{3/2}$ with the lower binding component located at 618.9 eV and is assigned to triiodide I^{3-} (Fig. 6a–c).[28] The shift to higher binding energy

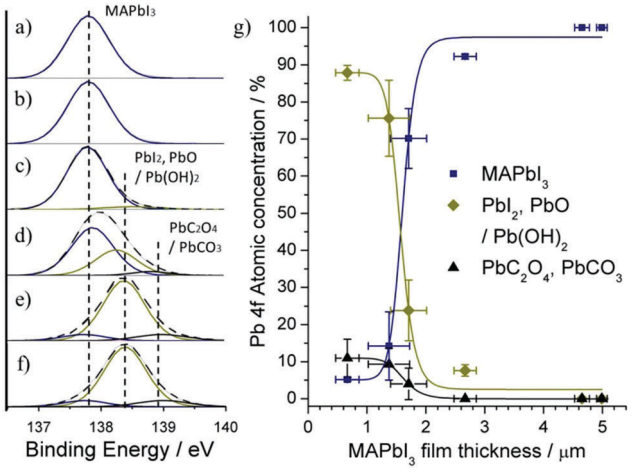

Fig. 5 (a) X-ray photoelectron spectroscopy analysis of the Pb 4f region for decreasing $MAPbI_3$ film thickness: (a) 4.99 μm, (b) 4.65 μm, (c) 2.67 μm, (d) 1.71 μm, (e) 1.37 μm, (f) 0.67 μm and (g) summarized atomic concentration percentages for each fitted component in the Pb 4f spectra.

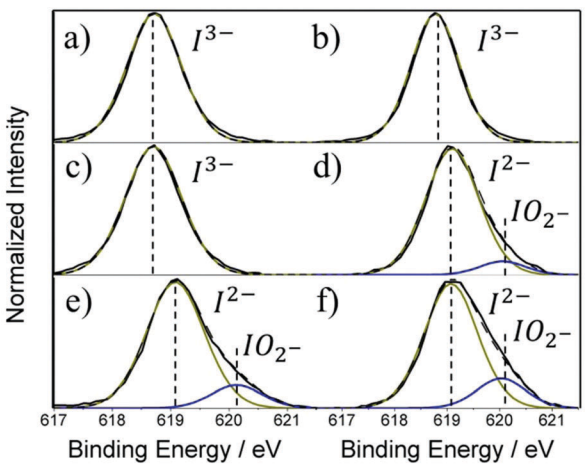

Fig. 6 XPS core level spectra for I 3d where (a–f) represents decreasing $MAPbI_3$ film thickness: (a) 4.99 μm, (b) 4.65 μm, (c) 2.67 μm, (d) 1.71 μm, (e) 1.37 μm and (f) 0.67 μm.

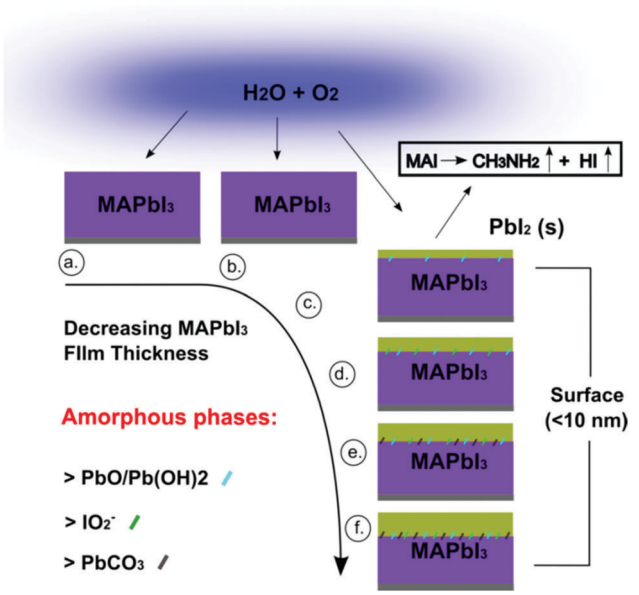

Fig. 7 Schematic highlighting the changing surface chemistry for $MAPbI_3$ films of decreasing thickness: (a) 4.99 μm, (b) 4.65 μm, (c) 2.67 μm, (d) 1.71 μm, (e) 1.37 μm and (f) 0.67.

619.1 eV (Fig. 6d–f) is associated with the loss of an iodide ion through MAI evaporation leaving the I^{2-} anion from PbI_2.[33] Additional broadening of the I 3d spectra for thinner $MAPbI_3$ films indicate the presence an additional peak at 620.2 eV that is credited to the oxidation of iodine at the surface which forms the I_2^+ cation and the iodite (IO_2^-) anion.[28,30,33]

Detailed XPS analysis of $MAPbI_3$ films clearly indicates that spraying thinner $MAPbI_3$ films allows for the formation of surface intermediate $MAPbI_{2+x}$ phases and finally surface PbI_2 on the very top-layer (Fig. 7). The loss of iodine ions through the breakdown of the MAI component is closely linked with the increase in oxygen concentration at the films surface. For thinner $MAPbI_3$ films, the concentration of adsorbed OH^- and O^{2-} ions increased relative to adventitious hydrocarbons (O═C and O═C–O) that are typically found on samples surface. These surface adsorbed species diffuse into the $MAPbI_3$ and cause distortion of the perovskites framework where the MA cation is easily dissociated due to its weak interaction with PbI_6 network. The destruction of the $MAPbI_3$ lattice and specifically the organic core is also evident through the decrease in N 1s atomic concentration (Fig. 2a) even before NH_x bonds are absent from the surface (see ESI†). The breakdown of the MAI component creates a number of iodine vacancies that can be easily terminated by intercalated oxygen species to create amorphous and constrained bonding arrangements such as $PbO/Pb(OH)_2$, IO_2^- and $PbCO_3/PbC_2O_4$. MAI can be further broken down into the volatile components CH_3NH_2 and HI and are evaporated leaving solid PbI_2 at the surface.

Surface morphology and grain analysis

SEM images of $MAPbI_3$ films show the changing surface morphology with decreasing film thickness (Fig. 8). The grains transition from large micro sized cube like structures typical of $MAPbI_3$ (Fig. 8a–c, thicker films) to de-agglomerated smaller distorted arrangements in thinner films (Fig. 8d–f) is evident, as the surface undergoes decomposition to $MAPbI_{2+x}/PbI_2$. Recent work involving density functional theory calculations have shown that defects, originating within the perovskites organic core, can be easily formed at room temperature.[39] The generation of these defects therefore enhances interactions with atmospheric species where it is understood that the deprotonation of MA cation is the first degradation step. The creation of intrinsic volatile components (HI & CH_3NH_2) and succeeding desorption process within the $MAPbI_3$ structure was shown to progressively erode the $MAPbI_3$ lattice.[40] Structural rearrangement of PbI_6 octahedral due to the loss of I atoms to volatile components MAI and HI allows for PbI_2 crystal seed to form simultaneously and gradually transform the $MAPbI_3$ lattice into PbI_2.[41] The deagglomeration of large micro sized $MAPbI_3$ grains (Fig. 8c–f) signifies this structural reorganization, occurring at the interface of $MAPbI_3$ crystallites or at lattice defects within the grains. The subsequent increase in surface roughness accelerates the degradation process where micro sized PbI_2 hexagonal structures being to form visibly at the surface (Fig. 8d and e). Quantitative grain analysis is performed for each film by selecting a small area with >15 grains (insets Fig. 8a–f) and using imageJ software. Plotting a histogram of grain size for each film (Fig. 8g) and a graph of grain size as a function of $MAPbI_3$ thickness (Fig. 8h), it is observed that grain size decreases significantly as the surface decomposes from $MAPbI_3$ to $MAPbI_{2+x}/PbI_2$. The size distribution of Fig. 8g has been fitted with Gaussian fits to produce mean size and standard deviation summarized in Fig. 8h. For sprayed films where the surface was experimentally determined to have I/Pb atomic mass close to 2 : 1, (Fig. 8d–f), the small distorted grains create a largely porous layer that presents a rough and non-uniform surface. This structural transformation and decreased grain sizes associated with PbI_2 formation has been observed in multiple works, regardless of deposition technique.[42–44]

Electronic band structure

Low binding energy XPS scans (Fig. 9a) for $MAPbI_3$ films with decreasing film thickness give insight into valence levels and can demonstrate more sensitivity to chemical interactions compared with core electrons. The XPS signal onset begins when highly kinetic/low binding photoelectrons from the outer most valence levels of $MAPbI_3$ are bombarded by the X-ray source, escaping to vacuum level and to the electron detector. Valence band spectra exhibits a broad signal in the range 0–6 eV that can be de-convoluted into two peaks corresponding to I 5p non-bonding state with a right shoulder peak assigned to the anti-bonding hybrid state of Pb 6s and I 5p state.[45,46] XPS analysis previously revealed that the total oxygen atomic concentration calculated from the integrated area under the core level O 1s increased for decreasing $MAPbI_3$ film thickness (Fig. 2a). After peak fitting the spectra it was specified that an increase in OH^- and O^{2-} ions was the main cause (Fig. 4), indicating that thinner $MAPbI_3$ films fabricated using one step spray method exhibited increased surface reactivity. The consequence of this increased

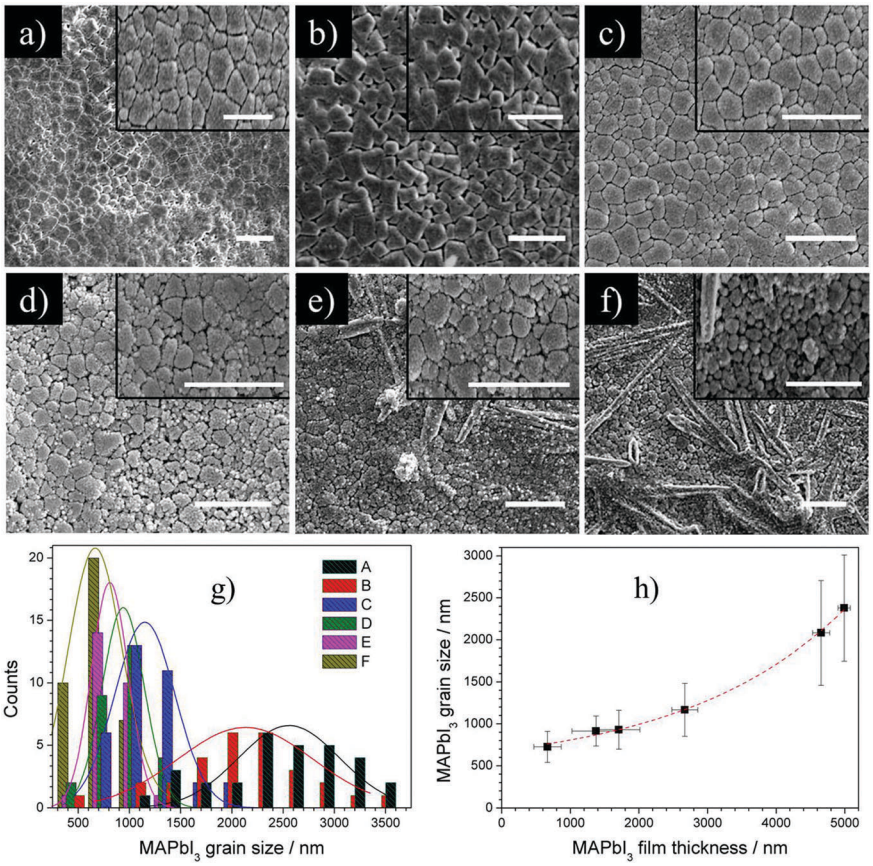

Fig. 8 Surface scanning electron microscopy (SEM) images of $MAPbI_3$ films at decreasing thickness: (a) 4.99 μm, (b) 4.65 μm, (c) 2.67 μm, (d) 1.71 μm, (e) 1.37 μm and (f) 0.67 μm. Insets show increased magnification images used for size analysis (all scale bars are set to 5 μm including insets). (g) Histogram of grain size analysis in the range 0–3750 nm and bin size 300 nm for films (a–f) with (h) plot of average grain size as a function of $MAPbI_3$ film thickness where error bars for *y*-axis represent the SD of measured grain sizes for films (a–h).

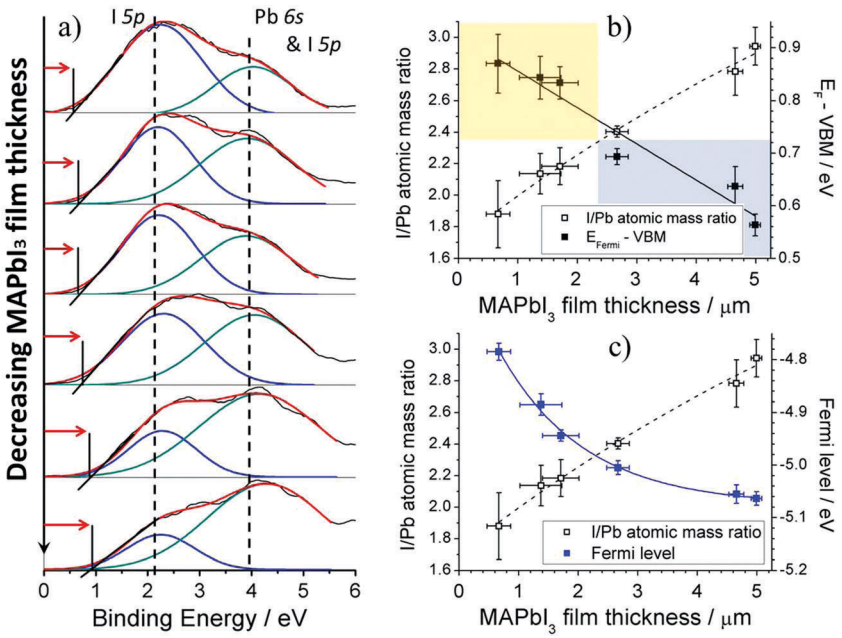

Fig. 9 (a) X-ray photoelectron spectroscopy (XPS) valence region scans for decreasing $MAPbI_3$ film thicknesses (4.99 μm, 4.65 μm, 2.67 μm, 1.71 μm, 1.37 μm, 0.67 μm) where E_f–VBM is valence band maximum energy relative to the Fermi energy (E_f). (b) E_f–VBM plotted as a function of $MAPbI_3$ film thicknesses and corresponding I/Pb atomic mass ratio. (c) Absolute Fermi level measurements determined using Kelvin probe plotted as a function of $MAPbI_3$ film thicknesses and corresponding I/Pb atomic mass ratio.

interaction resulted in the enhanced surface decomposition of $MAPbI_3$ to form $MAPbI_{2+x}$ through the evaporation of the MAI component. Once again it can be observed that reducing $MAPbI_3$ film thickness increases the concentration of Pb 6s and I 5p state anti-bonding hybrid state relative to I 5p non-bonding state. Additionally, the decomposition of $MAPbI_3$ to PbI_2 also shifts the onset of XPS signal to higher binding energies.

Extrapolating the XPS signal through the *x*-axis enables calculation of the valence band maximum (VBM) energy relative to the Fermi level (E_f) for the $MAPbI_3$ films. A number of studies have suggested that XPS-based measurements to determine VBM positions for air exposed $MAPbI_3$ films are more consistent and reproducible when compared to measurements derived from ultraviolet photoelectron spectroscopy, since the latter provides information only to a depth of only 0.5–1 nm whereas the former provides information up to a 10 nm penetration depth.[47–49] Therefore, XPS analysis minimizes effects of surface states due to contaminants on the electronic density of states profile since a larger penetration depth ensures measurement is more representative of bulk material properties. Plotting E_f–VBM for each of the $MAPbI_3$ films shows decreasing energy separation from nearly 0.9 eV to 0.55 eV when going from a degraded 2 : 1 (yellow) to a stoichiometric 3 : 1 (blue) for I : Pb atomic ratio (Fig. 9b); for convenience we included here also the I : Pb atomic ratio from Fig. 2b. This implies that the Fermi level and the valence band are shifting away from each other as the film thickness is reduced and therefore moving from thicker weakly p-doped film to a more n-type thinner films. Experimental studies have highlighted the effects of Pb and I vacancies in $MAPbI_3$ films and concluded that $MAPbI_3$ films that are MAI deficient/PbI_2 rich are typically n-doped whereas PbI_2 deficient/MAI rich films are p-doped and is in good agreement with our experimental results.[50,51]

The VBM values determined using XPS measurements give values relative to the Fermi level which displays the energy separation and direction of Fermi movement successfully. However in order to establish absolute VBM positions relative to vacuum level the Fermi level of $MAPbI_3$ films must be first determined. The Fermi level of $MAPbI_3$ films has been measured using a Kelvin probe (Fig. 9c) that measures the contact potential difference of material relative to a known work function reference, in this case gold (−5.1 eV). Plotting $MAPbI_3$ Fermi level against film thickness shows that for thicker $MAPbI_3$ (I : Pb = 3 : 1) the Fermi level is −5.05 eV and is agreeable with literature;[52] also here in this case we have included the I : Pb atomic ratio from Fig. 2b. Reducing the $MAPbI_3$ film thickness decreases the I : Pb ratio to around 2.5 : 1 meaning that a high number of MA and I vacancies are present at the film surface with consequent reduction (in absolute values) of the Fermi level to −5 eV. This confirms the effect of MA and I deficiencies, which promote n-doping behaviour in $MAPbI_3$ films. Decreasing film thickness further where the I : Pb atomic mass ratio is <2.2 : 1 causes a gradual decrease (in absolute value) in the Fermi level to around −4.8 eV. The initial slow shift of the Fermi level can be attributed to the loss of MA and I concentration and associated vacancies, however it is not until after PbI_2 begins to form on our film surface (I : Pb atomic ratio <2.2) that the Fermi level noticeably shifts. It should be emphasized that depending on the thickness of the PbI_2 surface layer there may be some Fermi level pinning from the underlying $MAPbI_3/PbI_2$ interface which can explain the gradual increase in Fermi level as the thickness of PbI_2 layer increases. As PbI_2 crystallizes and grows the influence of the underlying $MAPbI_3$ electronic states become less significant until the value of the Fermi level reduces (in absolute values) to that of pure PbI_2.

Photovoltaic performance of sprayed $MAPbI_3$ films

In order to understand the effect of the surface chemistry for spray deposited $MAPbI_3$ films, typical current density–voltage (*JV*) characteristics were measured under AM 1.5 illumination in air. An increase in current density (J_{SC}), open circuit voltage (V_{OC}) and overall power conversion efficiency (PCE) was observed for progressively thinner $MAPbI_3$ absorbers. The PCE increases exponentially from 0.83% to 5.23% with decreasing film thickness due to the matching of the $MAPbI_3$ carrier diffusion length (Fig. 10b). Examining individual parameters of our $MAPbI_3$ devices (V_{OC}, FF, J_{SC}) we find that the main reason for increased PCE is the significant increase in J_{SC} from 4.9 mA cm^{-2} to 22.3 mA cm^{-2} with the V_{OC} also increasing from 0.52 V to 0.73 V (Fig. 10c).

Depending on processing technique, diffusion lengths in the range 200–500 nm have been observed for $MAPbI_3$ films which closely match typical film thicknesses seen in high efficiency $MAPbI_3$ devices.[53] However for devices that have used spray coating, optimal thin films cannot be produced yet and thicker films are generally obtained. Also in our case, reducing the film thickness further to <500 nm using spray technique proved difficult and produced extremely porous films exhibiting small rod like structures assumed to be PbI_2 (ESI†). The incorporation of these low thickness films in PV devices resulted in shunting behavior that is attributed to the non-homogeneity of the sprayed film. The increased degradation for thin sprayed films (<500 nm) is in good agreement with trend of the surface chemical changes for decreasing $MAPbI_3$ films (Fig. 2, 4 and 5). Our thinnest sprayed MAPbI3 film (670 nm thickness) gave the greatest PCE of 5.23% due to the optimization of absorber thickness close to carrier diffusion lengths.

The consistently low FF of around 0.33 could be in principle improved considerably by including a hole transport material (HTM), where incorporation of Spiro-OMeTAD in perovskite based devices has shown efficiencies increase beyond 20%.[2,3] However, since the spray deposition method used in this technique is fairly novel and to better assess the band alignment and energy band level changes with respect to a known stable metal (*i.e.* Au), it was decided to first understand the surface chemistry of as deposited $MAPbI_3$ films before inclusion of sequential layers. As the inclusion of an HTM such as spiro-OMeTAD has been widely reported to improve device efficiency, we expect this to happen also for these sprayed $MAPbI_3$ films. In any case, as our work clearly point out, spray deposition still has to overcome degradation challenges before optimal thin perovskite films can be produced to be competitive with devices produced by

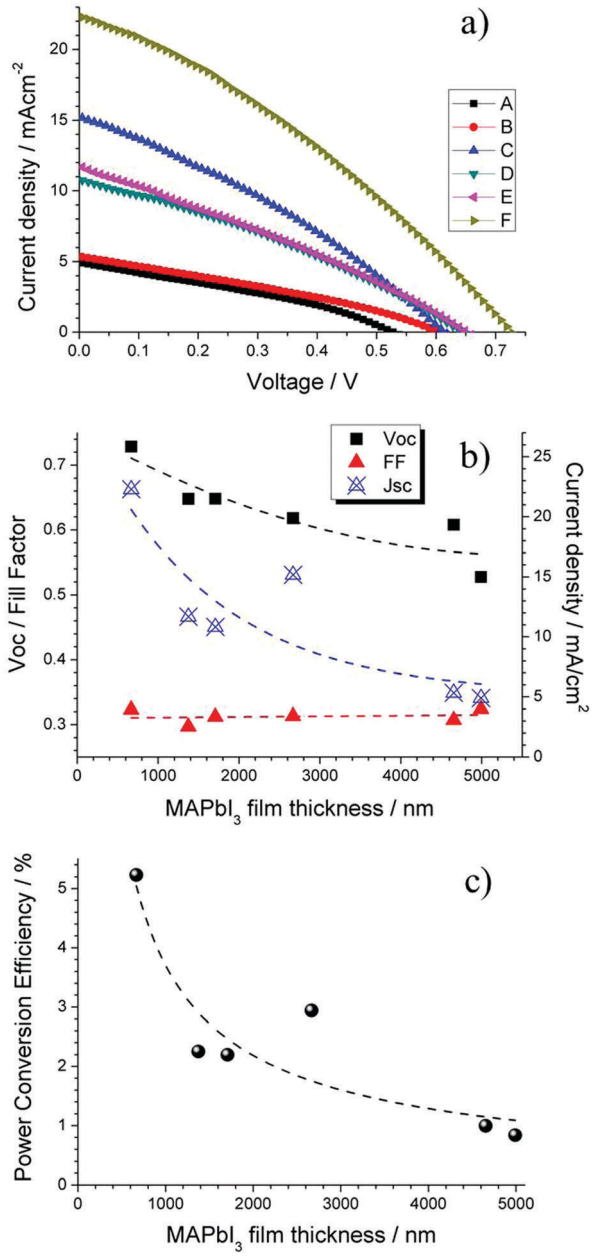

Fig. 10 (a) Illuminated current density–voltage characteristics of our devices with decreasing $MAPbI_3$ film thickness, (A–F) represents $MAPbI_3$ film thickness of (a) 4.99 μm, (b) 4.65 μm, (c) 2.67 μm, (d) 1.71 μm, (e) 1.37 μm and (f) 0.67 μm, (b) power conversion efficiency *vs.* decreasing $MAPbI_3$ film thickness and (c) individual device parameters V_{OC}, FF and J_{SC} *vs.* decreasing $MAPbI_3$ film thickness. Dotted lines are the result of exponential fitting using Origin software.

other methods. According to the equivalent circuit (ESI†), the *JV* characteristic can be described as

$$J = J_L - J_0\left[\exp\left(\frac{q(V + JAR_S)}{nk_BT}\right) - 1\right] - \frac{V + JAR_S}{AR_{sh}} \quad (1)$$

where J_L is the light induced constant current density, J_0 is the reverse saturated current density, R_S is the series resistance, R_{sh} is the shunt resistance, J is the current density flowing through the external load, n is the ideality factor, k_B is the Boltzmann constant, T is the absolute temperature, q is the elementary charge, A is the surface area of the cell and V is the direct-current (DC) bias voltage applied at the cell.[54] Based on eqn (1), some intrinsic parameters of our cells can be derived from the *JV* measurements. The first derivative of the voltage *vs.* current density can be used to extract useful parameters.

$$-\frac{dV}{dJ} = \frac{nk_BT}{q}(J_{SC} - J)^{-1} + AR_S \quad (2)$$

Fig. 11a shows the plots of $-dV/dJ$ *vs.* $(J_{SC} - J)^{-1}$ and the linear fitting curves according to eqn (2). Our cells show a linear relationship between $-dV/dJ$ and $(J_{SC} - J)^{-1}$ in the region approaching the V_{OC}. The area normalized series resistance (AR_S) of the cells can be deduced from the intercept of the linear fitting results in the region approaching $(J_{SC} - J)^{-1} = 0$.[55] We observe AR_S of our devices reducing from 33.4 Ω cm^2 to 7.2 Ω cm^2 with decreasing $MAPbI_3$ film thickness and as a consequence we observe a large increase in the devices J_{SC}. Additionally, the *JV* curves can be used to determine the voltage dependant ideality factor (n) of devices for values from 0 V up to the corresponding V_{OC} (Fig. 11b). When plotting the natural log of the current density against the voltage, the slope q/nk_BT gives a value for n.[56] In a heterojunction solar cell, values of n can give an insight into the

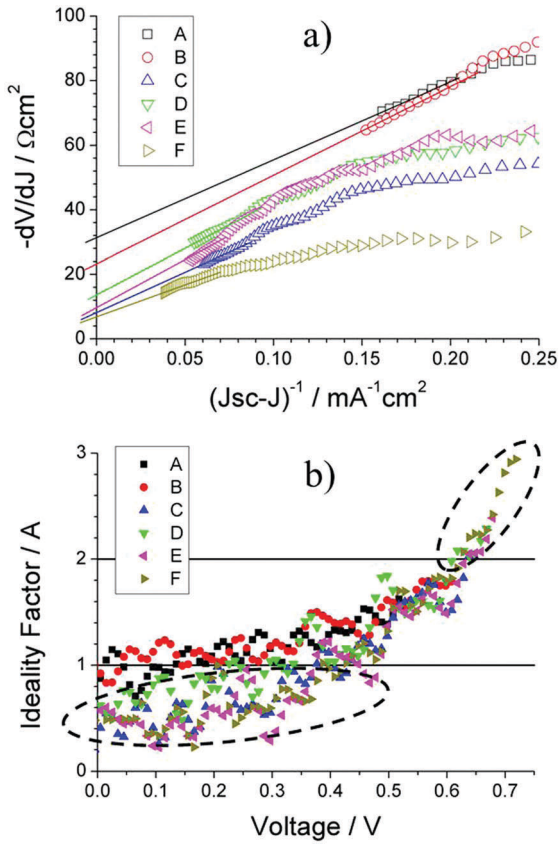

Fig. 11 (a) Plot of $-dV/dJ$ *vs.* $(J_{SC} - J)^{-1}$ for devices with decreasing $MAPbI_3$ film thickness and extrapolated linear fit near $(J_{SC} - J)^{-1} = 0$ (b) voltage dependant ideality factor of the devices with abnormally low and high values emphasized. (A–F) Represents $MAPbI_3$ film thickness of (a) 4.99 μm, (b) 4.65 μm, (c) 2.67 μm, (d) 1.71 μm, (e) 1.37 μm and (f) 0.67 μm.

quality of a junction and the carrier recombination mechanisms. The ideality factor is typically in the range $1 < n < 2$, for a "well-behaved" heterojunction.[56] When the junction is dominated by the carrier diffusion in the neutral region, n is at low values of 1. On the other hand, when carrier recombination in the depleted space charge region dominates the current, n is moving away from unity. In most cases, both carrier diffusion and recombination take place simultaneously.[55,56]

High values for ideality factor can also be caused by various other effects such as interface states, tunnelling processes and non-uniform distribution of interfacial charges.[57–59] More specifically interface dipoles due to interface doping as well as fabrication induced defects play an important role in the performance and reliability of metal/semiconductor structures.[60] Looking at Fig. 11b, we see that n increases with voltage approaching V_{OC} for each device. For the two devices with the greatest $MAPbI_3$ film thickness (black squares/red circles), the ideality factor is between values of 1 to 2 in the range 0 V to the device V_{OC}. As we reduce our $MAPbI_3$ film thickness within our solar cell, we see that the value of n beings to exceed 2 in the region approaching each devices specific V_{OC} and falls below 1 at voltages <0.3 V. Ideality factor moving away from unity approaching V_{OC} has previously been highlighted for $MAPbI_3$ HTM free solar cells[56,61] and suggests that the current is mainly controlled by the recombination in the space charge region of the TiO_2 and $MAPbI_3$ layers. However, ideality factors above 2 have been previously shown to be a clear indication of trap assisted tunnelling or field enhanced recombination through isolated point defects.[62,63]

Nonetheless, the highlighted areas suggest poor Schottky contact effect in our devices for thin $MAPbI_3$ films. The fact that decreasing $MAPbI_3$ film thickness produces smaller grain boundaries as highlighted earlier, may explain why the ideality factor drops below unity. The smaller grains/increased grain boundaries clearly increase the potential for recombination through surface states before carriers can be successfully collected at the back contact. Light soaking effects over a period of 0–6 min, including effect on individual parameters were collected (ESI†). Comparing light soaking effects on PCE for 3 devices that represent the maximum, minimum and intermediate $MAPbI_3$ absorber thickness (Fig. 12), a distinct trend can be observed. Thick $MAPbI_3$ film exhibits lowest PCE (<1%) most likely due to the thickness being larger than the carrier diffusion length; however with continued light soaking over a time period of 6 min the PCE significantly increases to more than 3%. For $MAPbI_3$ film with intermediate thickness (*i.e.* 2.67 μm) the beneficial light soaking effect is diminished and the PCE drops slightly from 2.9% to around 2% over the same time period. Finally for the thinner $MAPbI_3$ film (0.67 μm), the PCE at 0 min illumination is more than 5%. However increasing the time under illumination induces notable negative impact with the PCE decreasing from >5% to less than 2%.

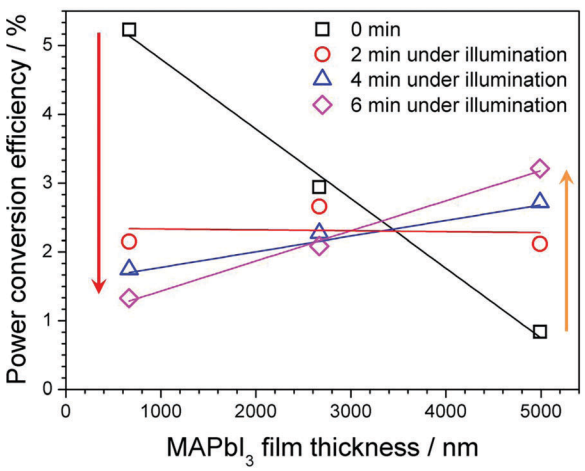

Fig. 12 Power conversion efficiency of devices with maximum, intermediate and minimum $MAPbI_3$ film thickness of 5 μm, 2.6 μm and 0.6 μm respectively, at 0 min, 2 min, 4 min and 6 min under illumination.

Discussion

PV performance of our thicker $MAPbI_3$ devices (~5 μm) showed a relatively low J_{SC} measured at 0 minutes (Fig. 10c) before increasing considerably after 6 min light soaking (4.9 mA cm^{-2} to 14 mA cm^{-2}, see ESI†), corresponding to the behaviour of the PCE (Fig. 12). This light soaking phenomena is generally observed for perovskite devices where the PCE is typically presented after stabilization at the maximum power point which takes place in a short time scale (0–3 min).[64,65] The stabilization period is understood to be caused by the filling of shallow charge trap sites by photo generated electrons or migrating ions, shifting the quasi-Fermi-level for electrons and therefore V_{OC} increases (Fig. 13, 0 min). The reduction in trap site density also increases J_{SC} accordingly due to the reduction in non-radiative pathways available.[64] Recently photo-induced brightening of $MAPbI_3$ photoluminescence was demonstrated and attributed to an order of magnitude reduction in trap state density due to migration of iodide ions.[7] Due to the high number of oxygen vacancies (V_O) that are expected in TiO_2, many of the photo excited carriers (e^-) may become trapped at the interface which can create electric fields and encourage iodide ion (I^-) migration.[66] The mobile iodide ions migrate away from the incident illumination into the $MAPbI_3$ film and fill iodide vacancies (V_I) that translate as shallow states below (above) the CBM (VBM) (Fig. 13, 2–4 min).[67]

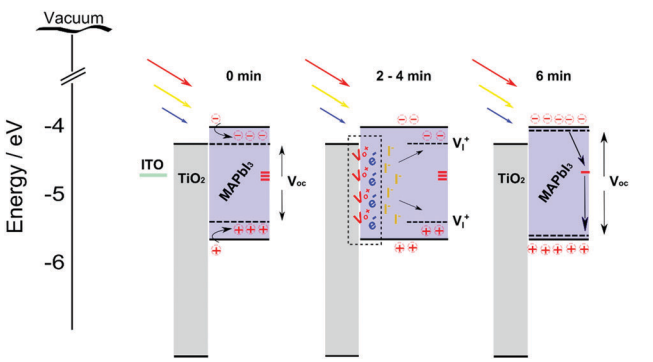

Fig. 13 Schematic showing the potential photo induced cleaning due to halide distribution that can explain light soaking stabilization period experienced in $MAPbI_3$ films under illumination.

The annihilation of these defects under increased light soaking would result in the shifting of quasi-Fermi level and the reduction of non-radiative recombination pathways, largely increasing open circuit voltage and photo carrier collection (Fig. 13, 6 min).

Depending on processing technique, diffusion lengths in the range 200–500 nm have been observed for $MAPbI_3$ films which closely match typical film thicknesses seen in high efficiency $MAPbI_3$ devices.[53] Therefore, in order to optimize the photo generated current from spray deposited $MAPbI_3$ films presented in this work, absorber thickness was reduced to around the same magnitude of carrier diffusion lengths. Decreasing the $MAPbI_3$ film thickness increased overall carrier collection as a substantial increase in PV performance at 0 minutes is observed for devices (Fig. 10b and c). It is known that $MAPbI_3$ films are susceptible to chemical decomposition that originates from chemisorbed or dissociated oxygen species and XPS analysis has highlighted that this modification is accelerated at the surface of thin spray-coated films with the increase of OH^-/O^{2-} surface species. Energy bands are displayed for $MAPbI_3$ films of decreasing thickness and changing surface chemistry (Fig. 14). Figure labels (a–f) correspond to varying film thickness of 4.99 μm, 4.65 μm, 2.67 μm, 1.71 μm, 1.37 μm and 0.67 μm, respectively. XPS, Kelvin probe and UV-Vis measurements correlate well to show that reduced PbI_2 on the surface creates a type-1 hetero-junction with the underlying $MAPbI_3$. Energy levels presented here are non-equilibrated however it is evident that a significant potential barrier would exist for hole extraction at the back electrode (Fig. 14c–f). This is in agreement with a previous report that claimed a type-1 alignment of PbI_2 with $MAPbI_3$ (VB and CB located at −5.75 and −3.45 eV) and a potential barrier of 30–50 mV.[68]

From theoretical simulations, the majority of defects in $MAPbI_3$ have low formation energies and create shallow levels within the bandgap,[67] which are unlikely to influence our Fermi level measurements. However these theoretical simulations were carried out on the assumption of pure perovskite phases. It is important to note however that the formation of different phases at the surface of $MAPbI_3$ films, such as those highlighted in this study (*i.e.* PbI2, Fig. 14c–f), can result in low energy/deep defect states and potentially influence the Fermi levels determined experimentally in this work.[69] Moreover, these defect states can provide mid gap levels at which carriers can recombine thus suppressing carrier collection at the back electrode.

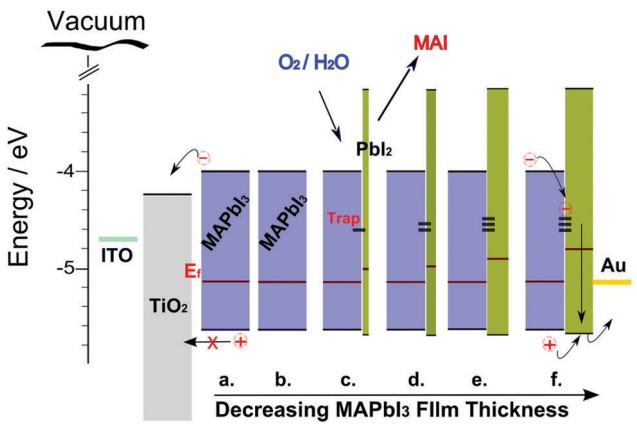

Fig. 14 Energy band structures for our device architectures showing changes in surface chemistry and how subsequent electron transfer process may be affected for decreasing $MAPbI_3$ film thickness: (a) 4.99 μm, (b) 4.65 μm, (c) 2.67 μm, (d) 1.71 μm, (e) 1.37 μm and (f) 0.67 μm. Energy level are non-equilibrated. The absolute values of the band edges and Fermi levels for the $MAPI_3$ and PbI_2 layer are taken from our experimental measurements (Fig. 9b and c) and bandgap values from literature.

Counter to the beneficial light soaking effects observed for $MAPbI_3$ devices in this work (for thicker films, Fig. 12 and 14a, b) and also in the literature, we notice a contradictory trend for spray-coated thin films (Fig. 12 and 14c–f) that we attribute directly to the changing surface chemistry and subsequent defect states at the back electrode. A $MAPbI_{2+x}$ film (I/Pb atomic ratio = 2.5 : 1) whose surface (<10 nm) has been degraded from the initial stoichiometric crystal showed a decrease in J_{SC} over a period of 0–6 min under illumination (15.15 mA cm^{-2} to 13.86 mA cm^{-2}). This decrease in PV performance correlates directly with the changing surface chemistry where an increase in adsorbed oxygen species has resulted in the decomposition of $MAPbI_3$ structure. This instability under light soaking is exacerbated for a number of thinner films that show an initially high PCE before J_{SC} and V_{OC} significantly decrease over a period of 6 min. More specifically, a device incorporating a film with measured thicknesses of 0.67 μm showed the greatest PCE of 5.23% which decreased to 1.3% after 6 minutes continuous light soaking (Fig. 12). The quantified surface composition determined from XPS measurements showed an overall increase in O 1s atomic mass that was explicitly due to intercalated OH^- and O^{2-} species originating from adsorbed atmospheric species. The different morphologies are the determining factor for the surface chemistry where the increased surface to volume ratio that exist for thinner $MAPbI_3$ sprayed films imposes a large degree of surface stress and strain which limits the chemical stability under ambient conditions. In turn, the formation of different grain size distributions is a consequence of the aerosol droplet size and velocity distributions which affect how the droplets coalescence and subsequently evaporate on the dynamic growing surface. These factors are in turn influenced by input parameters (solution composition, gas flow and spraying conditions) and the evolving topography and thermal properties of the surface. Present results show that, for thinner $MAPbI_3$ films, a morphology with larger surface area increases the surface interactions with ambient atmospheric species, which are most likely responsible for a higher density of surface defects. These defects originate during the spray process annealing stage which allows the continuous adsorption of atmospheric species. The increased adsorption and interaction of OH^-/O^{2-} species leads to distortion of the perovskite lattice where the MA cation is originally dissociated due to weak van der Waals bonds with PbI_6 network. Recent work has highlighted that water vapour reactions, which lead to the formation of $MAPbI_3$–H_2O and $MAPbI_3$–$2H_2O$ hydrate phases and consequential hysteresis in solar devices, are reversible.[70] Water molecules form hydrogen bonds with surface halide, however no proton transfer happens unlike the situation with adsorbed OH radicals and OH^- species, where accelerated

perovskite decomposition has been shown to occur.[70] The resulting hydrogen/proton extraction from the surface MA cations forming surface CH_3NH_2 is suggested as the initial step in the degradation process with further breakdown producing NH_2 and HI components. The former can be easily evaporated whereas the latter can react with O_2 to form I_2 and H_2O or decompose into I_2 and H_2.[71] The same degradation path is evident here due to the experimentally observed decrease in both N 1s and I 3d atomic mass concentrations in addition to the Pb 4f core level shifting to a higher binding energies associated with the loss of iodide ions.

The interplay between oxygen and $MAPbI_3$ films has been well documented where films have exhibited poor morphologies and incomplete surface coverage under high oxygen concentrations. The distorted grain structure among inferior crystallinity observed in $MAPbI_3$ films in this study is clear evidence of oxygen detrimental effect on chemical stability. Moreover, electron–hole recombination lifetimes have been shown to dramatically shorten with increasing oxygen concentration along with substantial quenching of photoluminescence,[29,72] suggesting that intercalated oxygen species may act as deep trap centres for photo excited carriers. The high ideality factors demonstrated for thin $MAPbI_3$ films (Fig. 11b) indicated poor Schottky contact effect and trap assisted recombination at the back electrode. The fact that devices, where surface decomposition (<10 nm) has occurred ($MAPbI_3$ to $MAPbI_{2+x}/PbI_2$), exhibit good PV performance initially at 0 minutes before the photocurrent and open circuit voltage are degraded under continued light soaking (0–6 minute) suggests that trap sites become filled before consequently forming macroscopic charged regions, increasing the potential barrier between bulk $MAPbI_3$ and surface PbI_2.

Conclusion

A rapid one step spray technique that possesses the potential for large scale manufacture has been implemented to fabricate $MAPbI_3$ absorber films with varying thickness and corresponding power conversion efficiencies from 0.83% to 5.22%. Investigation into the stability of devices under constant illumination showed conflicting behaviour with low efficiency (thick) $MAPbI_3$ films and high efficiency (thin) $MAPbI_3$ films, where the former displayed large increases in overall performance compared to rapid reductions experienced in the latter. It was experimentally concluded that the surface modification was directly related to instability of device performance under light soaking conditions. Determination of the Fermi level showed a net upward shift near the surface when transitioning from pristine $MAPbI_3$ to $MAPbI_{2+x}/PbI_2$. The measured energy separation E_f–VBM showed a comparable increase resulting in a potential barrier at the back contact that would significantly imped hole extraction. It was predicted however that the combined effect of intercalated OH^-/O^{2-} species, constrained amorphous states and dangling bonds due to I vacancies created a high density of shallow and deep level trap states that assisted in the non-radiative recombination of carriers. The spray deposition process demonstrated in this work can accelerate surface modification for thin films which is detrimental to PV performance under light soaking. Overall, this study suggests that deposition by spray method may enhance interactions of the solution being sprayed with atmosphere oxygen. The deployment of spray technologies will therefore need to take into account and reduce such detrimental impact. Future work will involve improvement of the one-step spray technique for $MAPbI_3$ thin film deposition for use in high efficiency solar cells among other applications.

Acknowledgements

This work has been partially funded by the Leverhulme Trust (IN-2012-136) and the EPSRC (EP/K022237/1 and EP/M024938/1). CR would like to acknowledge the support for the Northern Ireland Department for Employment and Learning (DEL). This work was also partially supported by a NEDO Project (Japan).

References

1 R. Fan, Y. Huang, L. Wang, L. Li, G. Zheng and H. Zhou, The Progress of Interface Design in Perovskite-Based Solar Cells, *Adv. Energy Mater.*, 2016, 1600460.
2 J. Burschka, N. Pellet, S.-J. Moon, R. Humphry-Baker, P. Gao, M. K. Nazeeruddin and M. Grätzel, Sequential Deposition as a Route to High-Performance Perovskite-Sensitized Solar Cells, *Nature*, 2013, **499**(7458), 316–320.
3 M. Liu, M. B. Johnston and H. J. Snaith, Efficient Planar Heterojunction Perovskite Solar Cells by Vapour Deposition_web, *Nature*, 2013, **501**(7467), 395–398.
4 S. A. Kulkarni, T. Baikie, P. P. Boix, N. Yantara, N. Mathews and S. Mhaisalkar, Band-Gap Tuning of Lead Halide Perovskites Using a Sequential Deposition Process, *J. Mater. Chem. A*, 2014, **2**, 9221.
5 C. Liu, J. Fan, X. Zhang, Y. Shen, L. Yang and Y. Mai, Hysteretic Behavior upon Light Soaking in Perovskite Solar Cells Prepared via Modified Vapor-Assisted Solution Process, *ACS Appl. Mater. Interfaces*, 2015, **7**(17), 9066–9071.
6 Y. Deng, Z. Xiao and J. Huang, Light-Induced Self-Poling Effect on Organometal Trihalide Perovskite Solar Cells for Increased Device Efficiency and Stability, *Adv. Energy Mater.*, 2015, **5**(20), 1–6.
7 D. W. deQuilettes, W. Zhang, V. M. Burlakov, D. J. Graham, T. Leijtens, A. Osherov, V. Bulović, H. J. Snaith, D. S. Ginger and S. D. Stranks, Photo-Induced Halide Redistribution in Organic–inorganic Perovskite Films, *Nat. Commun.*, 2016, **7**, 11683.
8 S. Meloni, T. Moehl, W. Tress, M. Franckevičius, M. Saliba, Y. H. Lee, P. Gao, M. K. Nazeeruddin, S. M. Zakeeruddin, U. Rothlisberger and M. Graetzel, Ionic Polarization-Induced Current–voltage Hysteresis in $CH_3NH_3PbX_3$ Perovskite Solar Cells, *Nat. Commun.*, 2016, **7**, 10334.
9 B. Wu, K. Fu, N. Yantara, G. Xing, S. Sun, T. C. Sum and N. Mathews, Charge Accumulation and Hysteresis in Perovskite-Based Solar Cells: An Electro-Optical Analysis, *Adv. Energy Mater.*, 2015, **5**(19), 1–8.

10 A. A. Bakulin, O. Selig, H. J. Bakker, Y. L. A. Rezus, C. Müller, T. Glaser, R. Lovrincic, Z. Sun, Z. Chen, A. Walsh, J. M. Frost and T. L. C. Jansen, Real-Time Observation of Organic Cation Reorientation in Methylammonium Lead Iodide Perovskites, *J. Phys. Chem. Lett.*, 2015, **6**(18), 3663–3669.

11 J. H. Heo, D. H. Song, H. J. Han, S. Y. Kim, J. H. Kim, D. Kim, H. W. Shin, T. K. Ahn, C. Wolf, T.-W. Lee and S. H. Im, Planar $CH_3NH_3PbI_3$ Perovskite Solar Cells with Constant 17.2% Average Power Conversion Efficiency Irrespective of the Scan Rate, *Adv. Mater.*, 2015, **27**(22), 3424–3430.

12 F. Polarization, N. H. Pbi, H. Kim, S. K. Kim, B. J. Kim, K. Shin, M. K. Gupta, H. S. Jung, S. Kim and N. Park, Ferroelectric Polarization in $CH_3NH_3PbI_3$ Perovskite, *J. Phys. Chem. Lett.*, 2015, **6**, 1729–1735.

13 J. Haruyama, K. Sodeyama, L. Han and Y. Tateyama, First-Principles Study of Ion Diffusion in Perovskite Solar Cell Sensitizers, *J. Am. Chem. Soc.*, 2015, **137**(32), 10048–10051.

14 O. Malinkiewicz, A. Yella, Y. H. Lee, G. M. M. Espallargas, M. Graetzel, M. K. Nazeeruddin and H. J. Bolink, Perovskite Solar Cells Employing Organic Charge-Transport Layers, *Nat. Photonics*, 2014, **8**(2), 128–132.

15 C.-C. Chen, Z. Hong, G. Li, Q. Chen, H. Zhou and Y. Yang, One-Step, Low-Temperature Deposited Perovskite Solar Cell Utilizing Small Molecule Additive, *J. Photonics Energy*, 2015, **5**(1), 057405.

16 H.-L. Hsu, C.-P. Chen, J.-Y. Chang, Y.-Y. Yu and Y.-K. Shen, Two-Step Thermal Annealing Improves the Morphology of Spin-Coated Films for Highly Efficient Perovskite Hybrid Photovoltaics, *Nanoscale*, 2014, **6**(17), 10281–10288.

17 Q. Chen, H. Zhou, Z. Hong, S. Luo, H.-S. Duan, H.-H. Wang, Y. Liu, G. Li and Y. Yang, Planar Heterojunction Perovskite Solar Cells via Vapor-Assisted Solution Process, *J. Am. Chem. Soc.*, 2014, **136**(2), 622–625.

18 Z. Song, S. C. Watthage, A. B. Phillips and M. J. Heben, Pathways toward High-Performance Perovskite Solar Cells: Review of Recent Advances in Organo-Metal Halide Perovskites for Photovoltaic Applications, *J. Photonics Energy*, 2016, **6**(2), 22001.

19 W. Hwang, G. Xin, M. Cho, S. M. Cho and H. Chae, Electrospray Deposition of Polymer Thin Films for Organic Light-Emitting Diodes, *Nanoscale Res. Lett.*, 2012, **7**(1), 52.

20 S. F. Tedde, J. Kern, T. Sterzl, J. Fürst, P. Lugli and O. Hayden, Fully Spray Coated Organic Photodiodes, *Nano Lett.*, 2009, **9**(3), 980–983.

21 M. Shao, S. Das, K. Xiao, J. Chen, J. K. Keum, I. N. Ivanov, G. Gu, W. Durant, D. Li and D. B. Geohegan, High-Performance Organic Field-Effect Transistors with Dielectric and Active Layers Printed Sequentially by Ultrasonic Spraying, *J. Mater. Chem. C*, 2013, **1**(28), 4384.

22 C. Girotto, D. Moia, B. P. Rand and P. Heremans, High-Performance Organic Solar Cells with Spray-Coated Hole-Transport and Active Layers, *Adv. Funct. Mater.*, 2011, **21**(1), 64–72.

23 R. C. Tenent, T. M. Barnes, J. D. Bergeson, A. J. Ferguson, B. To, L. M. Gedvilas, M. J. Heben and J. L. Blackburn, UItrasmooth, Large-Area, High-Uniformity, Conductive Transparent Single-Walled-Carbon-Nanotube Films for Photovoltaics Produced by Ultrasonic Spraying, *Adv. Mater.*, 2009, **21**(31), 3210–3216.

24 G. Grancini, V. D'Innocenzo, E. R. Dohner, N. Martino, A. R. Srimath Kandada, E. Mosconi, F. De Angelis, H. I. Karunadasa, E. T. Hoke and A. Petrozza, $CH_3NH_3PbI_3$ Perovskite Single Crystals: Surface Photophysics and Their Interaction with the Environment, *Chem. Sci.*, 2015, **6**(12), 7305–7310.

25 A. L. Abdelhady, M. I. Saidaminov, B. Murali, V. Adinolfi, O. Voznyy, K. Katsiev, E. Alarousu, R. Comin, I. Dursun, L. Sinatra, E. H. Sargent, O. F. Mohammed and O. M. Bakr, Heterovalent Dopant Incorporation for Bandgap and Type Engineering of Perovskite Crystals, *J. Phys. Chem. Lett.*, 2016, **7**(2), 295–301.

26 S. Barman and M. Sadhukhan, Facile Bulk Production of Highly Blue Fluorescent Graphitic Carbon Nitride Quantum Dots and Their Application as Highly Selective and Sensitive Sensors for the Detection of Mercuric and Iodide Ions in Aqueous Media, *J. Mater. Chem.*, 2012, **22**(41), 21832.

27 W. Huang, J. S. Manser, P. V. Kamat and S. Ptasinska, Evolution of Chemical Composition, Morphology, and Photovoltaic Efficiency of $CH_3NH_3PbI_3$ Perovskite under Ambient Conditions, *Chem. Mater.*, 2016, **28**(1), 303–311.

28 G. Rajendra Kumar, A. Dennyson Savariraj, S. N. Karthick, S. Selvam, B. Balamuralitharan, H.-J. Kim, K. K. Viswanathan, M. Vijaykumar and K. Prabakar, Phase Transition Kinetics and Surface Binding States of Methylammonium Lead Iodide Perovskite, *Phys. Chem. Chem. Phys.*, 2016, **18**(10), 7284–7292.

29 W. Kong, A. Rahimi-Iman, G. Bi, X. Dai and H. Wu, Oxygen Intercalation Induced by Photocatalysis on the Surface of Hybrid Lead Halide Perovskites, *J. Phys. Chem. C*, 2016, **120**(14), 7606–7611.

30 T.-W. Ng, C.-Y. Chan, M.-F. Lo, Z. Q. Guan and C.-S. Lee, Formation Chemistry of Perovskites with Mixed Iodide/chloride Content and the Implications on Charge Transport Properties, *J. Mater. Chem. A*, 2015, **3**(17), 9081–9085.

31 J.-H. Lee, N. C. Bristowe, P. D. Bristowe and A. K. Cheetham, Role of Hydrogen-Bonding and Its Interplay with Octahedral Tilting in $CH_3NH_3PbI_3$, *Chem. Commun.*, 2015, **51**(29), 6434–6437.

32 H. Xie, X. Liu, L. Lyu, D. Niu, Q. Wang, J. Huang and Y. Gao, Effects of Precursor Ratios and Annealing on Electronic Structure and Surface Composition of $CH_3NH_3PbI_3$ Perovskite Films, *J. Phys. Chem. C*, 2016, **120**(1), 215–220.

33 J. Zhang, T. Song, Z. Zhang, K. Ding, F. Huang and B. Sun, Layered Ultrathin PbI 2 Single Crystals for High Sensitivity Flexible Photodetectors, *J. Mater. Chem. C*, 2015, **3**(17), 4402–4406.

34 D. Chen, W. Shen, S. Wu, C. Chen, X. Luo and L. Guo, Ion Exchange Induced Removal of Pb(II) by MOF-Derived Magnetic Inorganic Sorbents, *Nanoscale*, 2016, **8**(13), 7172–7179.

35 J. M. Luther, M. Law, Q. Song, C. L. Perkins, M. C. Beard and A. J. Nozik, Structural, Optical, and Electrical Properties of Self-Assembled Films of PbSe Nanocrystals Treated with 1,2-Ethanedithiol, *ACS Nano*, 2008, **2**(2), 271–280.

36 C. H. Jo, J. H. Kim, J. Kim, J. Kim, M. S. Oh, M. S. Kang, M.-G. Kim, Y.-H. Kim, B.-K. Ju and S. K. Park, Low-Temperature Annealed PbS Quantum Dot Films for Scalable and Flexible Ambipolar Thin-Film-Transistors and Circuits, *J. Mater. Chem. C*, 2014, **2**(48), 10305–10311.

37 Z. Zheng, A. Liu, S. Wang, Y. Wang, Z. Li, W. M. Lau and L. Zhang, In Situ Growth of Epitaxial Lead Iodide Films Composed of Hexagonal Single Crystals, *J. Mater. Chem.*, 2005, **15**(42), 4555.

38 S. Rondon, Core Level and Valence Band Spectra of PbO by XPS, *Surf. Sci. Spectra*, 1998, **5**(2), 97.

39 I. Deretzis, A. Alberti, G. Pellegrino, E. Smecca, F. Giannazzo, N. Sakai, T. Miyasaka and A. La Magna, Atomistic Origins of $CH_3NH_3PbI_3$ Degradation to PbI2 in Vacuum, *Appl. Phys. Lett.*, 2015, **106**(13), 131904.

40 J. M. Frost, K. T. Butler, F. Brivio, C. H. Hendon, M. van Schilfgaarde and A. Walsh, Atomistic Origins of High-Performance in Hybrid Halide Perovskite Solar Cells, *Nano Lett.*, 2014, **14**(5), 2584–2590.

41 A. Alberti, I. Deretzis, G. Pellegrino, C. Bongiorno, E. Smecca, G. Mannino, F. Giannazzo, G. G. Condorelli, N. Sakai, T. Miyasaka, C. Spinella and A. La Magna, Similar Structural Dynamics for the Degradation of $CH_3NH_3PbI_3$ in Air and in Vacuum, *ChemPhysChem*, 2015, **16**(14), 3064–3071.

42 X. Tong, F. Lin, J. Wu and Z. M. Wang, High Performance Perovskite Solar Cells, *Adv. Sci.*, 2016, **3**(5), 1500201.

43 B. Philippe, B.-W. Park, R. Lindblad, J. Oscarsson, S. Ahmadi, E. M. J. Johansson and H. Rensmo, Chemical and Electronic Structure Characterization of Lead Halide Perovskites and Stability Behavior under Different Exposures—A Photoelectron Spectroscopy Investigation, *Chem. Mater.*, 2015, **27**(5), 1720–1731.

44 T.-B. Song, Q. Chen, H. Zhou, C. Jiang, H.-H. Wang, Y. (Michael) Yang, Y. Liu, J. You and Y. Yang, Perovskite Solar Cells: Film Formation and Properties, *J. Mater. Chem. A*, 2015, **3**(17), 9032–9050.

45 Y. Yuan, R. Xu, H.-T. Xu, F. Hong, F. Xu and L.-J. Wang, Nature of the Band Gap of Halide Perovskites ABX 3 (A = CH_3NH_3, Cs; B = Sn, Pb; X = Cl, Br, I): First-Principles Calculations, *Chin. Phys. B*, 2015, **24**(11), 116302.

46 H. Xu, Y. Wu, J. Cui, C. Ni, F. Xu, J. Cai, F. Hong, Z. Fang, W. Wang, J. Zhu, L. Wang, R. Xu and F. Xu, Formation and Evolution of the Unexpected PbI_2 Phase at the Interface during the Growth of Evaporated Perovskite Films, *Phys. Chem. Chem. Phys.*, 2016, **18**(27), 18607–18613.

47 B. Conings, L. Baeten, C. De Dobbelaere, J. D'Haen, J. Manca and H.-G. Boyen, Perovskite-Based Hybrid Solar Cells Exceeding 10% Efficiency with High Reproducibility Using a Thin Film Sandwich Approach, *Adv. Mater.*, 2014, **26**(13), 2041–2046.

48 E. M. Miller, Y. Zhao, C. C. Mercado, S. K. Saha, J. M. Luther, K. Zhu, V. Stevanović, C. L. Perkins and J. van de Lagemaat, Substrate-Controlled Band Positions in $CH_3NH_3PbI_3$ Perovskite Films, *Phys. Chem. Chem. Phys.*, 2014, **16**(40), 22122–22130.

49 R. Lindblad, D. Bi, B. Park, J. Oscarsson, M. Gorgoi, H. Siegbahn, M. Odelius, E. M. J. Johansson and H. Rensmo, Electronic Structure of TiO_2/CH_3NH_3 PbI_3 Perovskite Solar Cell Interfaces, *J. Phys. Chem. Lett.*, 2014, **5**(4), 648–653.

50 Q. Wang, Y. Shao, H. Xie, L. Lyu, X. Liu, Y. Gao and J. Huang, Qualifying Composition Dependent P and N Self-Doping in $CH_3NH_3PbI_3$, *Appl. Phys. Lett.*, 2014, **105**(16), 163508.

51 A. Naikaew, P. Prajongtat, M. C. Lux-Steiner, M. Arunchaiya and T. Dittrich, Role of Phase Composition for Electronic States in $CH_3NH_3PbI_3$ Prepared from $CH_3NH_3I/PbCl_2$ Solution, *Appl. Phys. Lett.*, 2015, **106**(23), 232104.

52 C. Bi, Y. Shao, Y. Yuan, Z. Xiao, C. Wang, Y. Gao and J. Huang, Understanding the Formation and Evolution of Interdiffusion Grown Organolead Halide Perovskite Thin Films by Thermal Annealing, *J. Mater. Chem. A*, 2014, **2**(43), 18508–18514.

53 G. W. P. Adhyaksa, L. W. Veldhuizen, Y. Kuang, S. Brittman, R. E. I. Schropp and E. C. Garnett, Carrier Diffusion Lengths in Hybrid Perovskites: Processing, Composition, Aging, and Surface Passivation Effects, *Chem. Mater.*, 2016, **28**(15), 5259–5263.

54 J. Xiao, J. Shi, D. Li and Q. Meng, Perovskite Thin-Film Solar Cell: Excitation in Photovoltaic Science, *Sci. China: Chem.*, 2015, **58**(2), 221–238.

55 S. S. Hegedus and W. N. Shafarman, Thin-Film Solar Cells: Device Measurements and Analysis, *Prog. Photovoltaics*, 2004, **12**(23), 155–176.

56 J. Shi, J. Dong, S. Lv, Y. Xu, L. Zhu, J. Xiao, X. Xu, H. Wu, D. Li, Y. Luo and Q. Meng, Hole-Conductor-Free Perovskite Organic Lead Iodide Heterojunction Thin-Film Solar Cells: High Efficiency and Junction Property, *Appl. Phys. Lett.*, 2014, **104**(6), 063901.

57 V. Lakshmi Devi, Schottky Barrier Parameters and Interfacial Reactions of Rapidly Annealed Au/Cu Bilayer Metal Scheme on N-Type InP, *Open Appl. Phys. J.*, 2012, **5**(1), 1–9.

58 R. T. Tung, Electron Transport at Metal–Semiconductor Interfaces: General Theory, *Phys. Rev. B*, 1992, **45**(23), 13509–13523.

59 W. Mönch, Barrier Heights of Real Schottky Contacts Explained by Metal-Induced Gap States and Lateral Inhomogeneities, *J. Vac. Sci. Technol., B: Microelectron. Nanometer Struct.*, 1999, **17**(4), 1867.

60 R. F. Schmitsdorf, Explanation of the Linear Correlation between Barrier Heights and Ideality Factors of Real Metal-Semiconductor Contacts by Laterally Nonuniform Schottky Barriers, *J. Vac. Sci. Technol., B: Microelectron. Nanometer Struct.*, 1997, **15**(4), 1221.

61 W. A. Laban and L. Etgar, Depleted Hole Conductor-Free Lead Halide Iodide Heterojunction Solar Cells, *Energy Environ. Sci.*, 2013, **6**(11), 3249.

62 O. Breitenstein, P. Altermatt, K. Ramspeck, M. A. Green, J. Zhao and A. Schenk, Interpretation of the Commonly Observed I-V Characteristics of C-SI Cells Having Ideality Factor Larger Than Two. In *2006 IEEE 4th World Conference on Photovoltaic Energy Conference*, IEEE, 2006, pp. 879–884.

63 A. Kaminski, J. J. Marchand, H. El Omari, A. Laugier, Q. N. Le and D. Sarti, Conduction Processes in Silicon Solar Cells. In *Conference Record of the Twenty FifthIEEE Photovoltaic Specialists Conference – 1996*, IEEE, 1996, pp. 573–576.

64 S. D. Stranks, V. M. Burlakov, T. Leijtens, J. M. Ball, A. Goriely and H. J. Snaith, Recombination Kinetics in Organic-Inorganic Perovskites: Excitons, Free Charge, and Subgap States, *Phys. Rev. Appl.*, 2014, **2**(3), 034007.

65 H. J. Snaith, A. Abate, J. M. Ball, G. E. Eperon, T. Leijtens, N. K. Noel, S. D. Stranks, J. T.-W. Wang, K. Wojciechowski and W. Zhang, Anomalous Hysteresis in Perovskite Solar Cells, *J. Phys. Chem. Lett.*, 2014, **5**(9), 1511–1515.

66 W. Zhang, S. Pathak, N. Sakai, T. Stergiopoulos, P. K. Nayak, N. K. Noel, A. A. Haghighirad, V. M. Burlakov, D. W. DeQuilettes, A. Sadhanala, W. Li, L. Wang, D. S. Ginger, R. H. Friend and H. J. Snaith, Enhanced Optoelectronic Quality of Perovskite Thin Films with Hypophosphorous Acid for Planar Heterojunction Solar Cells, *Nat. Commun.*, 2015, **6**, 10030.

67 W.-J. Yin, T. Shi and Y. Yan, Unusual Defect Physics in $CH_3NH_3PbI_3$ Perovskite Solar Cell Absorber, *Appl. Phys. Lett.*, 2014, **104**(6), 063903.

68 Q. Chen, H. Zhou, T.-B. Song, S. Luo, Z. Hong, H.-S. Duan, L. Dou, Y. Liu and Y. Yang, Controllable Self-Induced Passivation of Hybrid Lead Iodide Perovskites toward High Performance Solar Cells, *Nano Lett.*, 2014, **14**(7), 4158–4163.

69 C. C. Stoumpos, C. D. Malliakas and M. G. Kanatzidis, Semiconducting Tin and Lead Iodide Perovskites with Organic Cations: Phase Transitions, High Mobilities, and Near-Infrared Photoluminescent Properties, *Inorg. Chem.*, 2013, **52**(15), 9019–9038.

70 E. Mosconi, J. M. Azpiroz and F. De Angelis, Ab Initio Molecular Dynamics Simulations of Methylammonium Lead Iodide Perovskite Degradation by Water, *Chem. Mater.*, 2015, **27**(13), 4885–4892.

71 L. Zhang and P. H.-L. Sit, Ab Initio Study of Interaction of Water, Hydroxyl Radicals, and Hydroxide Ions with $CH_3NH_3PbI_3$ and $CH_3NH_3PbBr_3$ Surfaces, *J. Phys. Chem. C*, 2015, **119**(39), 22370–22378.

72 S. Yuan, Z. Qiu, H. Zhang, H. Gong, Y. Hao and B. Cao, Oxygen Influencing the Photocarriers Lifetime of $CH_3NH_3PbI_{3-x}Cl_x$ Film Grown by Two-Step Interdiffusion Method and Its Photovoltaic Performance, *Appl. Phys. Lett.*, 2016, **108**(3), 033904.

